Est. 1984

ORIENTAL JOURNAL OF CHEMISTRY
An International Open Free Access, Peer Reviewed Research Journal

www.orientjchem.org

ISSN: 0970-020 X
CODEN: OJCHEG
2013, Vol. 29, No. (1):
Pg. 113-120

Chemical Treatment, Characterization and Electrical Properties of Utilization Biowaste Hydroxyapatite Nanocrystalline

E.H.EL-MOSSALAMY*, L.M.AL-HARBI and A.Y.OBAID

Department of Chemistry, Faculty of Science,
King Abdulaziz University, 21589 Jeddah, P.O. Box 80203, Saudi Arabia.
*Corresponding author E-mail : sbdmina@yahoo.com

(Received: December 31, 2012; Accepted: February 27, 2013)

ABSTRACT

Hydroxyapatite (HAP) nanoparticles were successfully synthesized from the biowaste chicken bone and phosphoric acid solution by precipitation chemical route. The structures of HAP were characterized in terms of the X-ray diffraction (XRD), scanning electron microscope (SEM) and Fourier transform infrared spectroscopy (FTIR). The effect of temperature on the crystallinity and lattice parameters of as prepared HAP are monitored by X-ray powder diffraction. Energy Dispersive was revealed and determined also test as photo catalysis. The temperature dependence on the electrical conductivity of sintered HAP nanoparticles was investigated. Furthermore, dielectric properties such as dielectric constant and dielectric loss as a function of frequency of sintered HAP were studied.

Key words: HAP, Synthesis, IR, X-Ray, Nanoparticle.

INTRODUCTION

Functionalization of nonmaterial's with chemical or biological molecules exhibits novel properties for various potential applications. Synthetic hydroxyapatite, $Ca_{10}(PO_4)_6(OH)_2$ (HAP) is analogous to natural apatite, the major inorganic component of bone and teeth[1-10]. HAP has extensively been studied as filler for bulk bone regeneration and for improving oesteointegration of biomedical implants due to its bioactive and osteoconductive properties[11-15]. However, an important issue for in vivo application is its biocompatibility. When bone is lost due to injury, the defects are sometimes filled with natural bone. However, as natural bone is often of variable quality and if it is not from the same person as the recipient, it may lead to possible disease transmission. Synthetic HAP with well defined properties offers a good, safer alternative bone graft material which can help the body to repair bone defects[6,7]. Recently, HAP has found interesting applications in other areas such as a support for adsorption of bacteria or viruses, for ammonia catalysis, as a catalyst support material, support bone ingrowths and osseointegration when used in orthopaedic, dental and maxillofacial applications[16-20]. Thereof, the synthesis of HAP has been a major subject for chemists and material scientists for many years since it is one of the most important and versatile

bioceramics[21-26]. With the ever-growing need to develop clean, non-toxic and environmentally friendly techniques, HAP powders have been extracted using bio products like corals[1], cuttlefish shells[2], natural gypsum[3], natural calcite[4], bovine bone [5], etc. Chemical analysis has shown that these products which are otherwise considered as biowaste are rich sources of calcium in the form of carbonates and oxide. One of such biowastes is chicken eggshells. Everyday million tons of eggshells are generated as biowaste around the globe. Eggshell represents 11 % of the total weight of the egg and is largely composed of calcium carbonate (minerals calcite) 97 % and organic matter 3% [1-10]. This material is an unwanted byproduct after the production of eggs and egg derivatives. Normally, manufacturers and factories store the material or dispose of it as an unwanted polluting industrial residue[22,23].

EXPERIMENTAL

Preparation of HAP nanoparticles

Hydroxyapatite (HAP) nanoparticles were prepared by chemical precipitation via aqueous slurries comprising of biowaste chicken bone and phosphoric acid. In the first step, uncrushed and washed raw chicken bone were collected and mechanically cleaned,

Characterization

The crystal phase and structure of the samples were determined by X-ray diffraction (XRD) using a Shimadzu diffractometer (Shimadzu-Japan) Microstructure and chemical composition were determined using JEOL 6300 Scanning Electron Microscope (SEM) equipped with JEOL Electron Dispersive Spectrometer (EDS) at a 5 KV accelerating potential. Prior to Microstructure and chemical composition were determined using JEOL 6300 Scanning Electron Microscope (SEM) equipped with JEOL Electron Dispersive Spectrometer (EDS) at a 5 KV accelerating potential. Prior to observation, the surface of the samples was coated with a thin, electric conductive copper film. Fourier transformed infrared (FTIR) spectroscopy using FT-IR 1750 (Perkin-Elmer Instruments), Electrical conductivity was measured by the four-point probe method. Rectangular shape samples of dimensions 4 x 3 x 3 cm were cut from the sintered pellets and then coated with Indium electrodes. The dielectric properties such as dielectric constant and dielectric loss were carried out using RLC bridge (Grounding RLC- Germany)

RESULTS AND DISCUSSION

The HAP nanopowders were characterized by broad peaks with no secondary phases indicating that the synthesized HAP was pure and in a good match to JCPDS pattern 09-432) with a crystallite size of about 22nm as calculated using the Debye Scherrer equation. It is seen that the crystallinity of HAP nanopowders increased with heat treatment temperature. Fig.1(a-d) shows the XRD pattern of the HAP nanopowder calcined at different temperatures from 400^{0}C, 700^{0}C, 1000^{0}C and 1200 ^{0}C, respectively. Broad diffraction peaks were observed for the HAP powders heat-treated at 700 ºC. With increase in heat-treatment temperature, these diffraction peaks became sharper as expected, indicating the increase in crystallinity of HAP powders. Crystal structure refinements were carried out using X-ray diffraction data for qualitative and quantitative phase analyses. The Reitveld refinements confirm the formation of only phase pure HAP. Typical structure refinement patterns of green i.e. as prepared and sintered HAP at 1200 °C are shown in Figs. (2a) and (2b),respectively. The green HAP sample was heat-treated at different temperatures to assess phase stability [see Figs. (2a) and (2b)]. It is noted also that the HAP powders are stable at high temperatures and there was no secondary phase formation which is rather surprising compared to the literature.[10-15] The Reitveld refinements also confirm the stability of the HAP phase without any decomposition or formation of secondary phases (see Table 1 and Fig. 2b). Crystallite sizes were calculated from X-ray data and as expected, increasing heat- treatment temperature resulted in an increase in crystallite size, crystal structure at various temperatures are illustrated in Fig. (3). For the in situ XRD, it can be clearly seen that the a-axis decreases while c-axis increases with increasing temperature. Chemical composition analysis was carried out using EDS and the results are reported in Table 2. It was observed that the ratio Ca/P for both the green and heat-treated samples is *ca.* 1.69, which can be compared to a value of 1.67 which

would be expected for fully stiochiometric HAP. Figs. (4a) and (4c) show images of green and heat-treated HAP powder, respectively. Agglomerates of very fine particles were noticed [Fig. (4a)] for the green sample while after heat- treatment at 1200 °C, the particles become sub-100 micron in size [Fig. (4c)].

Crystallinity, Densification factor, surface area and flexural strength of green and heat treated of HAP at different temperature are reported in Table 3. Based on Table 3 results, higher of densification factor tend to harden the sintered HAP bodied to the interlocking of crystalline phase and plate-like microstructure of HAP.

The structure of the powder was analyzed using FT-IR spectroscopy after dried at 100 °C, as shown in Fig. (5). The FT-IR spectra exhibit distinct strong bands for green and heat-treated HAP (1200 °C for 2 hours). In the FT-IR analysis, mainly the peaks for PO_4^{3-} and OH^- groups in the hydroxyapatite

Table 1: Crystal structure refinements results using Fullprof program

	Lattice parameters		Atoms (Å)	Coordinates x	Occupancy y	z
Green HAP	a=9.413(1)	Ca1(4f)	1/3	1/3	0.001	1.008
	c=6.882(1)	Ca2(6h)	0.246(1)	-0.008(1)	1/4	0.994
		O1(6h)	0.328(1)	0.466(2)	1/4	1.038
		O2(6h)	0.595(2)	0.471(2)	1/4	0.994
		O3(12i)	0.334(1)	0.253(1)	0.081(1)	0.920
		O4(4e)	0.0	0.0	1/4	0.531
P1(6h)	0.409(2)	0.369(1)	1/4	0.982		
HAP 1200ºC	a=9.424(1)	Ca1(4f)	1/3	1/3	0.001	1.008
	c=6.887(1)	Ca2(6h)	0.245(1)	-0.005(1)	1/4	1.018
		O1(6h)	0.326(1)	0.475(2)	1/4	1.052
		O2(6h)	0.584(2)	0.469(2)	1/4	0.990
		O3(12i)	0.332(1)	0.250(1)	0.073(1)	0.940
		O4(4e)	0.0	0.0	1/4	0.516

Table 2: Chemical analysis using EDS technique

Elements	Ca	P	O	Ca/P
Green HAP	23.6(2)	14.2(1)	62.2(2)	1.65 (0.03)
HAP 1200ºC	23.8(2)	13.8(1)	62.3(2)	1.72 (0.03)

Table 3: Fraction of crystalline phase (X_c), Densification Factor (DF), Flexural Strength and Surface Area of HAP

Sample code	Crystallinity (%)	Crystallinity (%)	Crystallinity (%)	Surface area ($m^2 g^{-1}$)
Green HAP	52	52	52	82
HAP, 700 °C, 2h	59	59	59	84
HAP, 1000 °C, 2h	70	70	70	87
HAP, 1200 °C, 2h	77	77	77	90

can be identified in Fig. 6. These FTIR spectra reveal peaks similar to those expected for HAP [12]. The peak at 3571 cm^{-1} (strong) and 633 cm^{-1} correspond to the stretching mode (υ_s) and the liberational mode (υ_L) of hydroxyl, respectively. The peaks at 1430 and 1410 cm^{-1} correspond to stretching mode (υ_3) of carbonate in HA. The weak peak at 880 cm^{-1} corresponds to bending mode (υ_2) of carbonate which also diminishes at high temperatures analogous to the peaks at 1430 and 1410 cm^{-1}. Peaks at 602 and 564 cm^{-1} correspond to the bending mode (υ_4) of the O-P-O linkage. The temperature dependence of the electrical conductivity (σ) of heat-treated HAP up to 700 °C is shown in Fig. (6). Secondly, the increase of charge carrying proton density due to OH^- and O^{2-} leads to

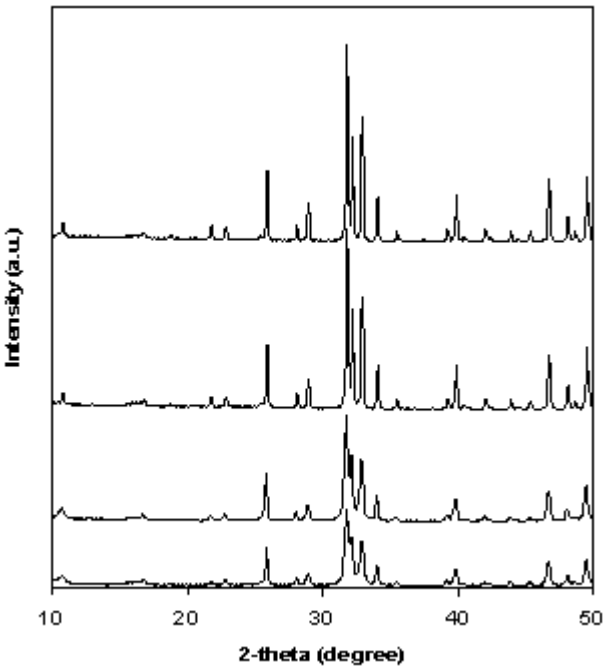

Fig. 1: X-ray diffraction patterns of as-prepared HAP (Green) and annealed samples at different temperatures

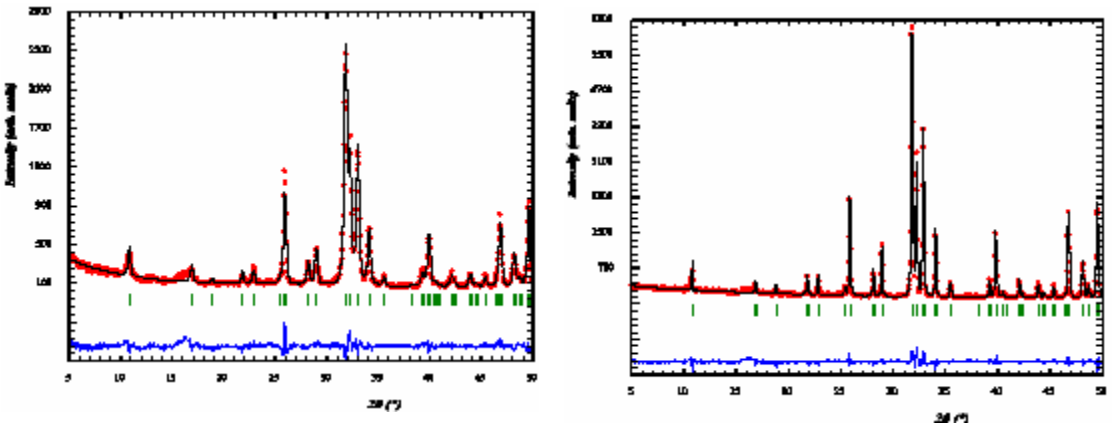

Fig. 2: Rietveld profile refinements of (a) green HAP and (b) HAP heat-treated at 1200ºC. Continuous line: calculated profile, empty circles o experimental recorded data, bottom line - : difference pattern of I_{obs} - I_{cal}, bottom line I : corresponds to positions of diffraction peaks

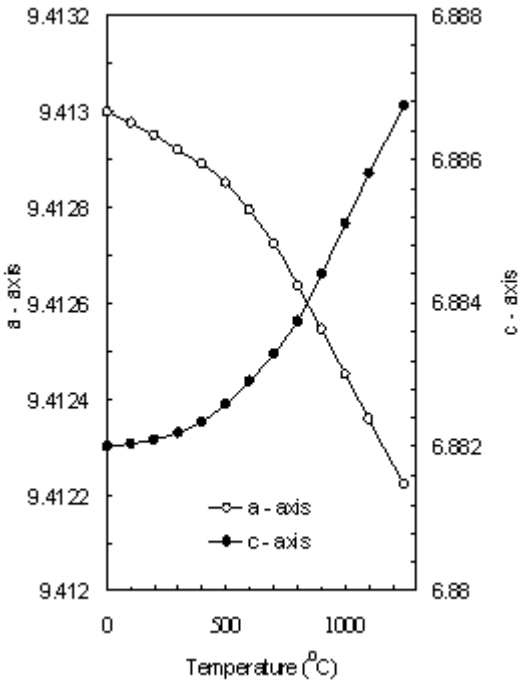

Fig. 3: Variation of lattice parameters a-axis and c-axis of green HAP with temperature as obtained from in situ powder X-ray diffraction measurements

the increase of conductivity as confirmed by FTIR analysis before. The conduction mechanism in HAP is due to either to a proton hopping along the c-axis between electro active O^{2-} anions, as follows:

$$OH^- + OH^- \leftrightarrow O^{2-} + HOH \quad ...(6)$$

And/or to an OH^- ions interacting with the double bonded oxygen of a PO_4^{3-} groups as follows:

$$OH^- + [PO_4]^- \leftrightarrow 0^{1-} + [HPO_4]^{2-} \xleftarrow{OH^-} O^{2-} + [PO_4]^- + HOH \quad ...(7)$$

In both cases, protons must be delocalized between O^{2-} anions in channels or PO_4^{3-} groups. Dehydration appears to be always initiated by thermally activated excess protons delocalized on the conduction. In this case, excess protons move through the lattice and become trapped onto OH^- lattice sites. H_2O molecules are formed which may eventually be repelled from the lattice, if they happen to be near the surface (or they can be re-dissolved in apatite structure). It is seen that the conductivity increases with increasing temperature.

At relatively low temperatures the electrical conductivity slightly increases. This can be explained as frozen equilibrium between defects and charge carriers. With increasing temperature, the conductivity rapidly increased. There are two possible reasons for increasing conductivity with temperature. Firstly, the hydroxyl ions migration through vacancies in the center of Ca ion triangle planes along the c-axis of the hexagonal structure of HAP. In addition, the transport of OH^- vacancies along the c-axis enhanced the conduction mechanism in the conductivity of HAP. On the basis of σ (T) obtained, the activation energy (E_a) of the charge conduction process can be determined according to the following equation[20]:

$$\sigma = \sigma_0 \, e^{-Ea/KT} \quad ...(8)$$

where σ stands for electric conductivity, σ_0 for pre-exponential factor, T for temperature, and K for the Boltzmann's constant.

The estimated value of E_a was *ca.* 1.77 eV and this was in good agreement with published data[14-16].

The hopping energy (E_h) was calculated using the following relation[19]:

$$\sigma\sqrt{T} = \sigma_0 \, e^{-Eh/KT} \quad ...(9)$$

The calculated value of E_h was about 2.91 eV. Notably, the value of E_a was much less than the value of . This strongly suggested that the conduction mechanism of HAP was governed by a proton hopping mechanism[21].

The dielectric constant and dielectric loss versus frequency for sintered HAP at 1250 °C is presented in Fig. 7. Notably, as we start increasing the frequency, both the dielectric constant and dielectric loss decrease. Dielectric absorption was not recorded beyond 10^6 Hz. There can be three possible reasons which evoked the observed decrease of both dielectric constant and loss with increasing frequency. Firstly, the relaxation time and ionic species of dielectric polarization are greatly reduced by increasing frequency, resulting in

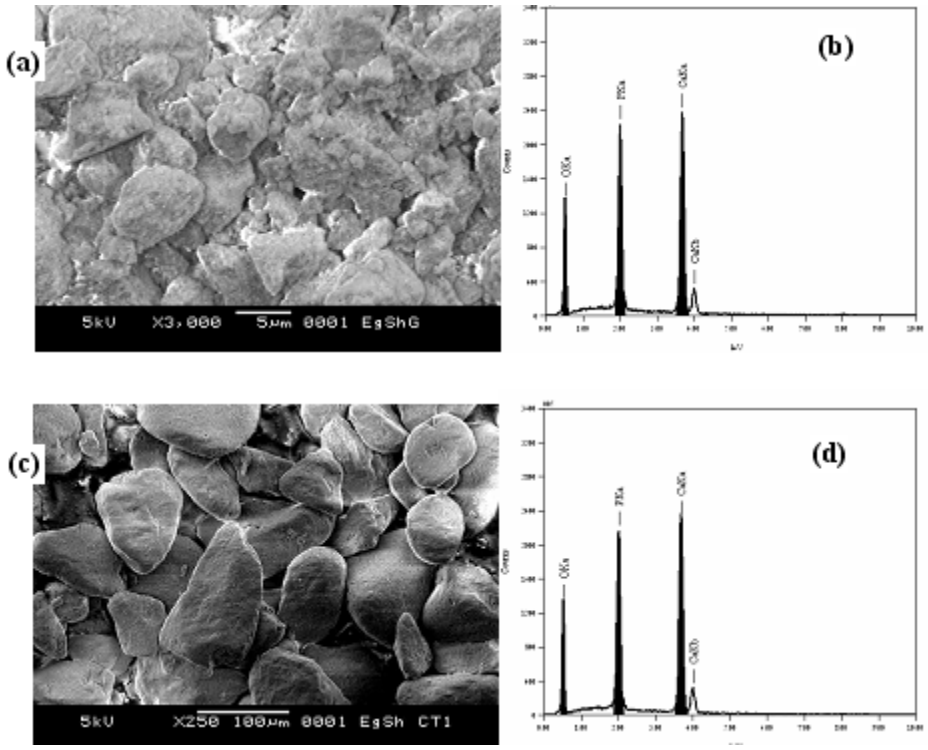

Fig. 4: SEM image of (a) as-prepared (Green) HAP, (b) its EDS spectrum, (b) SEM image of HAP sintered at T=1200ºC, and (d) its EDS spectrum

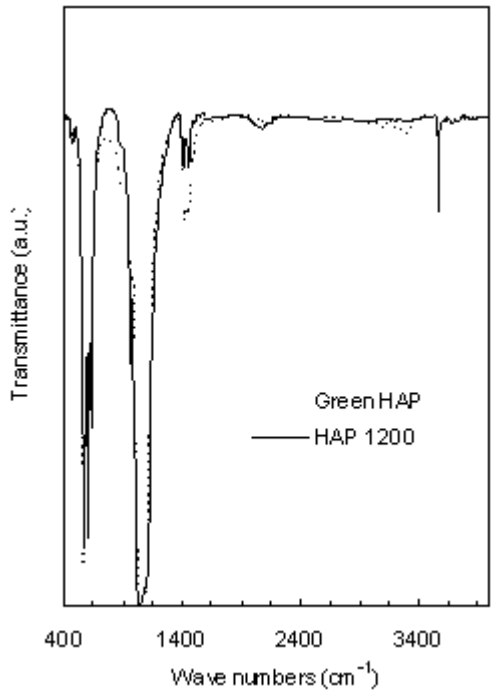

Fig. 5: Comparative study of FT-IR spectra of green HAP and HAP heat-treated at 1200°C for 2h

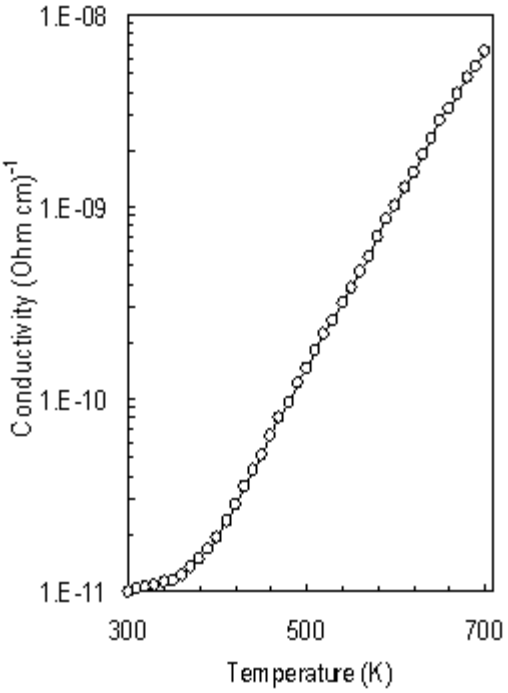

Fig. 6: Electrical conductivity versus temperature of sintered HAP particles

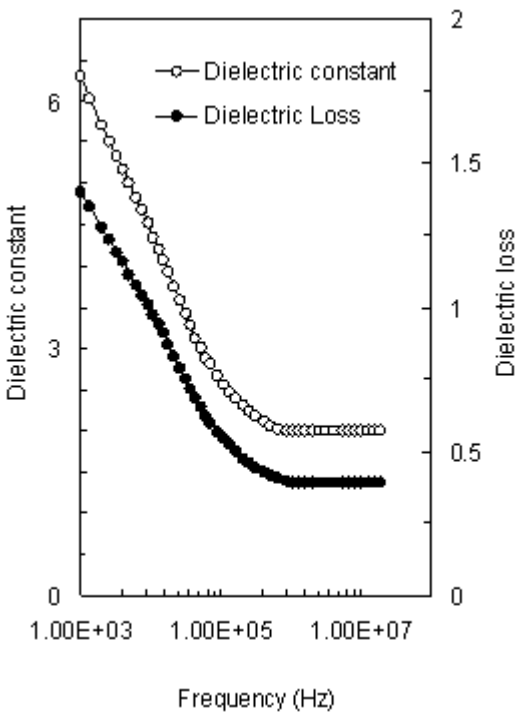

Fig. 7: Dielectric constant and dielectric loss versus frequency of sintered

decreasing both dielectric constant and dielectric loss. Secondly, the decrease of dielectric constant with frequency is due to the coulomb interactions of the charge carriers and the disorder within the structure, suggesting a Maxwell Wagner mechanism[26]. Thirdly, interfacial polarization is expected as dispersion occurs in the bulk properties from the charging of interfaces within the matrix.

CONCLUSION

Hydroxyapatite nanoparticles can successfully be produced by chemical precipitation technique from biowaste chicken bone and phosphoric acid solution as starting materials. Furthermore, the use of biowaste chicken bone via this method should also be applicable for the synthesis of other bioactive calcium phosphate and related biomedical materials. The temperature dependence of the electrical conductivity showed an increase with increasing temperature, except at low temperatures where a slight increase was observed. This was explained as frozen equilibrium between concentrations of defects and charge carriers. With increasing temperature, the conductivity rapidly increased and a likely conduction mechanism of a proton was proposed. The dielectric constant and dielectric loss decrease as a function of frequency with increasing frequency up to 10^6 Hz and then level off. This is due to the relaxation time and ionic species of dielectric polarization are greatly reduced by increasing the frequency.

ACKNOWLDGMENTS

This project was funded by the Deanship of Scientific Research (DSR), King Abdulaziz Univeristy, Jeddah, under grant no. (318 /13 ã .Ó /). The authors, therefore, acknowledge with thanks DSR for technical and financial support.

REFERENCES

1. C. Li, *Powder Technology*, **192:** 1 (2009).
2. Z. Wei, C. Xu, B. Li, *Bioresource Technology*, **100**: 2883 (2009).
3. C. Balazsi, F. Weber, Z. Kover, E. Horvath, C. Nemeth, *J. Eur. Ceram. Soc.*, **27**: 1601 (2007).
4. V. M. Rusu, C-H. Ng, M. Wilke, B. Tiersch, P. Fratzl, M. G. Peter, *Biomaterials,* **26**: 5414 (2005).
5. W. Zheng, X-M. Li , Q. Yang, G-M. Zeng, *J. Hazardous Materials*, **147**: 534 (2007).
6. K.P. Sanosh, M-C. Chu, A. Balakrishnan, T.N. Kim, S-J. *Cho, Materials Letters*, **63:** 2100 (2009).
7. G. Gergely, F. Weber, I. Lukacs, A. L. Toth, Z. E. Horvath, J. Mihaly, C. Balazsi*, Ceramics International,* **36**: 803 (2010).
8. K. Prabakaran, S. Rajeswari, *Spectrochimica Acta Part A,* **74**: 1127 (2009).
9. S. Yoo, J. S. Hsieh, P. Zou, J. Kokoszk, *Bioresource Technology*, **100**: 6416 (2009).
10. W. T. Tsai, J. M. Yang, C.W. Lai, Y.H. Cheng, C.C. Lin, C.W. Yeh*, Bioresource Technology*, **97**: 488 (2006).
11. E. M. Rivera, M. A. Araiza, W. Brostow, V. M. Catano, J. R. Diaz-Estrada, R. Rogelio, J. R. Rodriguez*, Materials Letters,* **41**: 128 (1999).
12. C. C. Silva, H. B. Rocha, F.N.A. Freire, M.R.P. Santos, K.D.A. Saboia, J.C. Goes, A.S.B. Sambra, *Mater. Chem. Phys.,* **92**: 260 (2005).
13. K. Prabakaban, A. Balamurugan, S. Rajeswari, *Bull. Mater. Sci. ,* **28**: 115 (2005).
14. S. V. Dorozhkin*, Acta Biomaterialia,* **6**: 715 (2010).
15. K. Zhu, K. Yanagisawa, A. Ondo, K. Kajiyoshi, *J. Solid State Chem.*, **177**: 4379 (2004).
16. S. J. Lee, S.H. Oh*. Materials Letters*, **57**: 4570 (2003).
17. Y.X. Pang, X. Bao, *J. Eur. Ceram. Soc.*, **23**: 1697 (2003).
18. S. Lazic, S. Zec, N. Miljevic, S. Milonjic, *Thermochim. Acta*, **374**: 13 (2001).
19. K. Ioku, S. Yamauchi, H. Fujimori, S. Goto, M. Yoshimura, *Solid Sate Ionics*, **151:** 147 (2002).
20. M.S. Khalil, H. Beheri, W. Abdel Fattah*, Ceram. Int.*, **28**: 451 (2002).
21. W.T. Tsai, J.M. Yang, C.W. Lai, Y.H. Cheng, C.C. Lin, C.W. Yeh*, Bioresource Technology,* **97**: 488 (2006).
22. H. Anmin, L. Tang, L. Ming, C. Chenkang, L. Huiqin, M.Dali*, Appl. Catal.,* **63:** 41 (2006).
23. I. Mobasherpour, M. S. Heshajin, A. Kazemzadeh, M. Zakeri, J*. Alloys Comp.*, **430**: 330 (2007).
24. A. Laghzizil, N. Elherch, A. Bouhaouss, G. Lorente, T. Coradin, J. Livage*, Mater. Res. Bull.*, **36**: 953 (2001).
25. L. Kubisz, S. Mielcarek, F. Jaroszyk, *Int. J. Biol. Macromol.,* **33**: 89 (2003).
26. F. Chen, Z.C. Wang, C.L. Lin, *Materials Letters*, **57**: 858 (2002).